Supplement of

Measurement Report: Optical and structural properties of atmospheric water-soluble organic carbon in China: Insights from multi-site spectroscopic measurements

5 Haibiao Chen[1,2], Caiqing Yan[1], Liubin Huang[1], Lin Du[1,3], Yang Yue[3], Xinfeng Wang[1], Qingcai Chen[4], Mingjie Xie[2], Junwen Liu[5], Fengwen Wang[6], Shuhong Fang[7], Qiaoyun Yang[8], Hongya Niu[9], Mei Zheng[10], Yan Wu[3], Likun Xue[1]

[1]Qingdao Key Laboratory for Prevention and Control of Atmospheric Pollution in Coastal Cities, Environment Research Institute, Shandong University, Qingdao 266237, China

10 [2]Collaborative Innovation Center of Atmospheric Environment and Equipment Technology, Jiangsu Key Laboratory of Atmospheric Environment Monitoring and Pollution Control (AEMPC), Nanjing University of Information Science & Technology, Nanjing 210044, China

[3]School of Environmental Science and Engineering, Shandong University, Qingdao 266237, China

[4]School of Environmental Science and Engineering, Shaanxi University of Science and Technology, Xi'an, 710021, China

15 [5]Institute for Environmental and Climate Research, Jinan University, Guangzhou 511443, China

[6]State Key Laboratory of Coal Mine Disaster Dynamics and Control, Department of Environmental Science, Chongqing University, Chongqing 400030, China

[7]College of Resources and Environment, Chengdu University of Information Technology, Chengdu 610225, China

[8]Department of Occupational and Environmental Health, School of Public Health, Tianjin Medical University, Tianjin 300070, China

20 [9]Key Laboratory of Resource Exploration Research of Hebei Province, Hebei University of Engineering, Handan 056038, China

[10]SKL-ESPC, College of Environmental Sciences and Engineering, and Center for Environment and Health, Peking University, Beijing, 100871, China

25 *Correspondence to*: Caiqing Yan (cyan0325@sdu.edu.cn)

Text S1. Determination of primary and secondary organic carbon.

The concentrations of primary organic carbon (POC) and secondary organic carbon (SOC) are estimated by the EC-tracer method as follows,

$$SOC = OC - EC \times (OC/EC)_{min} \tag{S1}$$

$$POC = OC - SOC \tag{S2}$$

where $(OC/EC)_{min}$ is the minimum OC/EC ratio during the sampling period at each site.

Text S2. Calculation of light absorption parameters.

The light absorption coefficient (Abs_λ, Mm^{-1}) of WSOC at the wavelength λ is calculated as follows,

$$Abs_\lambda = (A_\lambda - A_{700}) \times \frac{V_l}{V_a \times L} \times \ln(10) \tag{S3}$$

where V_l (mL) is the volume of the water extracts, V_a (m^3) is the air volume corresponding to the extracted sample filter, and L is the optical path length (1 m in this study). A_λ is the absorbance at wavelength λ measured by the spectrophotometer. A_{700} is chosen to reduce the effects of baseline drift and $\ln(10)$ is used to convert the absorption coefficient from log base 10 to natural logarithm. In this study, Abs_{365} is chosen as a proxy for the absorbance of WS-BrC to exclude the interferences of other substances (e.g., nitrate, etc.) (Hecobian et al., 2010).

The mass absorption efficiency (MAE, $m^2 \cdot g^{-1}$) of WSOC is calculated as follows,

$$MAE_\lambda = \frac{Abs_\lambda}{C_{WSOC}} \tag{S4}$$

where C_{WSOC} ($\mu g \cdot m^{-3}$) represents the mass concentration of WSOC.

The wavelength dependence of light absorption fits a power law as follows,

$$Abs_\lambda = K \times \lambda^{-AAE} \tag{S5}$$

where K is a constant related to light absorption and AAE is the absorption Ångström exponent used to characterize the wavelength dependence of WSOC light absorption. In this study, AAE is fitted over the wavelengths of 330-400 nm.

The imaginary part (k) of the particle refractive index ($m = n + ik$) is an important parameter that evaluates the light-absorbing efficiency of aerosols. In this study, we calculate the k_{405} using equation S6 and used $Log_{10}(MAE_{405})$ *vs.* AAE to classify different light-absorbing BrC (Saleh, 2020). To unify and facilitate comparison, the MAE_{365} values reported in previous studies are converted to MAE_{405} by the following equations (Liu et al., 2013; Saleh, 2020),

$$k_\lambda = \frac{MAE_\lambda \times \lambda \times \rho}{4\pi} \tag{S6}$$

$$k_{365} = k_\lambda \left(\frac{\lambda}{365}\right)^w \tag{S7}$$

$$w = AAE - 1 \tag{S8}$$

where ρ is particle density and assign as 1.5 $g \cdot cm^{-3}$ in this study.

55 **Text S3. Estimation of direct radiative effect of water-soluble brown carbon.**

Simple forcing efficiency (SFE) represents the energy added to the Earth-atmosphere system by a given mass of particles (Bond and Bergstrom, 2006). In this study, $d\text{SFE}(\lambda)/d\lambda$ (W·m^{-2}·nm^{-1}) and integrated SFE (W·g^{-1}, 300-400 nm and 300-700 nm) are calculated by following equations to estimate the direct radiative forcing of water-soluble brown carbon (Chen and Bond, 2010),

60
$$\frac{d\text{SFE}}{d\lambda} = -\frac{1}{4}\frac{d\text{S}(\lambda)}{d\lambda}\ \tau_{\text{atm}}^2(\lambda)\ (1 - \text{F}_\text{c})\left[2(1 - \alpha_\text{s})^2\ \beta(\lambda)\ \text{MAE}(\lambda) - 4\alpha_\text{s}\ \text{MAE}(\lambda)\right] \tag{S9}$$

$$\text{SFE} = \int_\lambda \frac{d\text{S}(\lambda)}{d\lambda}\ \tau_{\text{atm}}^2(\lambda)\ (1 - \text{F}_\text{c})\ \alpha_\text{s}\ \text{MAE}(\lambda)\ d\lambda \tag{S10}$$

where $d\text{S}(\lambda)/d\lambda$ is the solar irradiance (W·m^{-2}·nm^{-1}) obtained from the ASTM G173-03 reference spectra, τ_{atm} is the atmospheric transmission (0.79), Fc is the cloud fraction (0.6), α_s is the surface albedo (average 0.19), β is the backscatter fraction, MAE is the mass absorption efficiency of WSOC, respectively. It should be noted that only light absorption is considered and therefore 65 $\beta = 0$ in the calculation in this study.

Text S4. Light absorption spectra resolved by positive matrix factorization (PMF) model.

The positive matrix factorization (PMF) model is performed on the light absorption spectra of WSOC using the EPA PMF method (version 5.0). The rationale and detailed descriptions can be found in the PMF 5.0 Fundamentals and User Guide on the EPA website (https://www.epa.gov/air-research/epa-positive-matrix-factorization-50-fundamentals-and-user-guide). In 70 this study, absorbance data in the wavelength range of 250 to 400 nm (interval 5 nm) and corresponding uncertainties are included in the PMF analysis. The absorbance data below the method detection limit (MDL, 1.0 mAu in this study) are replaced by 1/2 MDL (Li et al., 2023b). The uncertainty (Unc) is calculated according to the following equations when the absorbance ≤ MDL (equation S11) and the absorbance > MDL (equation S12), respectively,

$$\text{Unc} = 5/6\ \text{MDL} \tag{S11}$$

75
$$\text{Unc} = \sqrt{(\text{Error Fraction} \times \text{absorbance})^2 + (0.5 \times \text{MDL})^2} \tag{S12}$$

where the error fraction is set as 0.2 in this study.

In this study, the sampling sites are classified into east China sites (QD, NJ, SH, TS) and outside east China sites (TJ, HD, XA, CD, CQ, HS) according to their distribution areas. Additionally, the absorption spectra have obvious regional characteristics, with the absorption spectra at outside east China sites showing obvious absorption peaks at 265 and 300 nm, while these 80 absorption peaks do not exist at east China sites (see Figure 5). PMF analysis is conducted on the absorbance datasets collected in two regions of China separately. Finally, four and three factors are resolved for east China sites and outside east China sites, respectively (see Figure S8).

Text S5. PARAFAC analysis and calculation of fluorescence parameters.

All the excitation emission matrices (EEMs) data are normalized by the water Raman peak area (Ex = 350 nm, Em = 385-410 nm) and the data are ultimately presented in Raman units (RU) (Lawaetz and Stedmon, 2009). Parallel factor analysis (PARAFAC) with the non-negativity constraint of Raman normalized EEMs data is performed using the DOMFluor toolbox (v 1.7) in MATLAB R2020a to identify the potential fluorophores (Stedmon and Bro, 2008). Besides, fluorescent indices are calculated to provide source and structure information of atmospheric organic aerosols. The fluorescence index (FI), biological index (BIX) and humidification index (HIX) are determined according to the following equations (Wu et al., 2021), respectively.

$$FI = \frac{F(E_x = 370 \text{ nm}, E_m = 450 \text{ nm})}{F(E_x = 370 \text{ nm}, E_m = 500 \text{ nm})} \tag{S13}$$

$$BIX = \frac{F(E_x = 310 \text{ nm}, E_m = 380 \text{ nm})}{F(E_x = 310 \text{ nm}, E_m = 430 \text{ nm})} \tag{S14}$$

$$HIX = \frac{F(E_x = 255 \text{ nm}, E_m = 435\text{-}480 \text{ nm})}{F(E_x = 255 \text{ nm}, E_m = 300\text{-}345 \text{ nm})} \tag{S15}$$

It should be noted that FI (BIX) refers to the ratio of emission intensity of 450 and 500 nm (380 and 430 nm) at Ex = 370 nm (310 nm), while HIX is calculated with the integrated intensity over the wavelength range of 435-480 nm and 300-345 nm at Ex = 255 nm. In this study, these fluorescent indices are calculated by the EFC software (v 1.2) (Bro, 1997; He and Hur, 2015; Murphy et al., 2010; Stedmon and Bro, 2008; Zepp et al., 2004).

Moreover, the total fluorescence volume (TFV; RU-nm^2) and fluorescence volume (FV; RU-nm^2) of each fluorophore are calculated by integrating the Raman normalized EEMs data in MATLAB R2020a.

Text S6. Methods for extreme gradient boosting (XGBoost).

The extreme gradient boosting (XGBoost) model is a gradient-boosting-based ensemble algorithm that improves traditional techniques with remarkable attributes, including efficiency, precision, stability, and scalability (Li et al., 2024). In this study, XGBoost is used to evaluate the contribution of conventional air pollutants (CO, SO$_2$, O$_3$, NO$_2$) and fluorescent components to the light absorption coefficient (Abs$_{365}$). The national air quality data comes from the real-time release platform of the China Environmental Monitoring Station for urban air quality nationwide (https://quotsoft.net/air/). To further quantify the contributions of the target factors, the SHAP algorithm is introduced, which evaluates the feature contributions based on the marginal contributions of individuals in cooperative games (Li et al., 2024). The main formulas as following,

$$f(x) = \varphi_0(f, x) + \sum_{i=1}^{k} \varphi_i(f, x) \tag{S16}$$

$$\varphi_i(f, x) = \sum_{S \subseteq F \setminus \{i\}} \frac{|S|!(k-|S|-1)!}{k!} (f_x(S \cup \{i\}) - f_x(S)) \tag{S17}$$

where $\varphi_0(f, x)$ denotes the expected value of the light absorption coefficient predicted by the model on the training set. k is the

number of factors influencing the model. $\varphi_i(f, x)$ can be interpreted as the impact of the i-th factor on the prediction of the model when given an input x.

All operations are performed in Python 3.10 using Jupyter as an integrated coding environment. The following Python packages are used in this study: *scikit-learn* provides a standard interface for implementing machine learning algorithms, *pandas* and *NumPy* for data analysis process, *BayesSearchCV* for parameter optimization, *matplotlib* for data visualization, and *SHAP* for sensitivity analysis (Li et al., 2024).

Table S1. Summary of the sampling information.

Sites	Location	Region	Sampling period	Sample size	Sampling duration	Sampler	Filter
Tianjin (TJ)	39.11°N, 117.19°E	north China	2019/11/29 to 2020/01/06	41	23.5 h	medium-volume (100 L min^{-1}) sampler (TH-150A, Wuhan Tianhong, China)	QMA, Φ90 mm, (Whatman, USA)
Handan (HD)	36.57°N, 114.50°E		2019/12/26 to 2020/01/01	16	11.5 h	medium-volume (100 L min^{-1}) sampler (TH-150A, Wuhan Tianhong, China)	QMA, Φ90 mm, (Whatman, USA)
Qingdao (QD)	36.35°N, 120.67°E	east China	2019/11/11 to 2019/12/27	46	23.5 h	medium-volume (100 L min^{-1}) sampler (TH-150A, Wuhan Tianhong, China)	QMA, Φ90 mm, (Whatman, USA)
Nanjing (NJ)	32.21°N, 118.71°E		2019/12/02 to 2019/12/31	51	11 h	high-volume (300 L min^{-1}) sampler (ASM-1, Guangzhou Mingye, China)	QMA, 8×10 in, (Munktell, SE)
Shanghai (SH)	31.17°N, 121.44°E		2020/12/01 to 2020/12/28	20	22 h	high-volume (1.13 m^3 min^{-1}) sampler (Tisch Environment, USA)	QMA, 8×10 in, (Whatman, USA)
Xi'an (XA)	34.38°N, 108.98°E	northwest China	2019/11/21 to 2019/12/20	30	23.5 h	high-volume (1 m^3 min^{-1}) sampler (XT-1025, Shanghai Xintuo, China)	QMA, 8×10 in, (Whatman, USA)
Chengdu (CD)	30.58°N, 103.99°E	southwest China	2019/11/23 to 2020/01/04	37	23.5 h	medium-volume (100 L min^{-1}) sampler (TH-150A, Wuhan Tianhong, China)	QMA, Φ90 mm, (Whatman, USA)
Chongqing (CQ)	29.56°N, 106.45°E		2019//12/24 to 2020/01/08	17	23.5 h	high-volume (300 L min^{-1}) sampler (ASM-1, Guangzhou Mingye, China)	QMA, 8×10 in, (Whatman, USA)
Mt. Tai (TS)	36.25°N, 117.10°E	regional site	2019/12/05 to 2020/01/02	49	11.5 h	medium-volume (60 L min^{-1}) sampler (LY-2030, Qingdao Laoying, China)	QMA, Φ90 mm, (Whatman, USA)
Heshan (HS)	22.74°N, 112.95°E		2019/11/11 to 2020/01/21	15	24 h	high-volume (1 m^3 min^{-1}) sampler (XT-1025, Shanghai Xintuo, China)	QMA, 8×10 in, (Whatman, USA)

Table S2. Mass concentrations and related ratios of carbonaceous components measured in this study.

Sites	Regions	OC (μg·m⁻³) Avg ± SD	EC (μg·m⁻³) Avg ± SD	WSOC (μg·m⁻³) Avg ± SD	OC/EC Avg ± SD	WSOC/OC (%) Avg ± SD	POC (μg·m⁻³) Avg ± SD	SOC (μg·m⁻³) Avg ± SD
Tianjin	north China	10.02 ± 6.06	1.20 ± 0.53	5.96 ± 3.21	7.99 ± 2.08	59.88 ± 11.75	5.64 ± 2.47	4.38 ± 3.94
Handan		17.87 ± 8.56	2.44 ± 0.48	10.56 ± 5.33	7.06 ± 2.52	55.24 ± 13.32	8.79 ± 1.72	9.08 ± 7.34
Qingdao	east China	8.69 ± 5.60	1.34 ± 0.83	4.68 ± 3.01	6.45 ± 1.15	55.05 ± 11.60	5.86 ± 3.62	2.83 ± 2.49
Nanjing		10.63 ± 4.16	2.36 ± 0.83	6.82 ± 2.00	4.58 ± 0.93	65.23 ± 11.86	7.03 ± 2.48	3.61 ± 2.84
Shanghai		3.31 ± 1.48	0.35 ± 0.16	1.97 ± 0.83	10.05 ± 2.69	60.98 ± 6.99	1.72 ± 0.79	1.59 ± 0.94
Xi'an	northwest China	17.76 ± 7.24	2.86 ± 1.49	10.24 ± 4.55	6.90 ± 1.65	57.26 ± 6.93	12.90 ± 6.74	4.87 ± 2.37
Chengdu	southwest China	12.19 ± 4.48	1.87 ± 0.51	8.98 ± 3.09	6.44 ± 1.41	73.26 ± 10.03	6.02 ± 1.63	6.17 ± 3.22
Chongqing		19.59 ± 6.48	2.25 ± 0.79	10.54 ± 3.45	9.02 ± 1.94	53.41 ± 4.94	13.63 ± 4.78	5.96 ± 3.98
Mt. Tai	regional site	4.17 ± 2.73	0.71 ± 0.74	3.60 ± 1.22	6.97 ± 3.11	65.08 ± 19.59	1.91 ± 2.00	2.26 ± 1.58
Heshan		9.17 ± 3.54	1.38 ± 0.31	5.85 ± 2.12	6.45 ± 1.52	64.39 ± 11.91	5.37 ± 1.20	3.80 ± 2.55

120
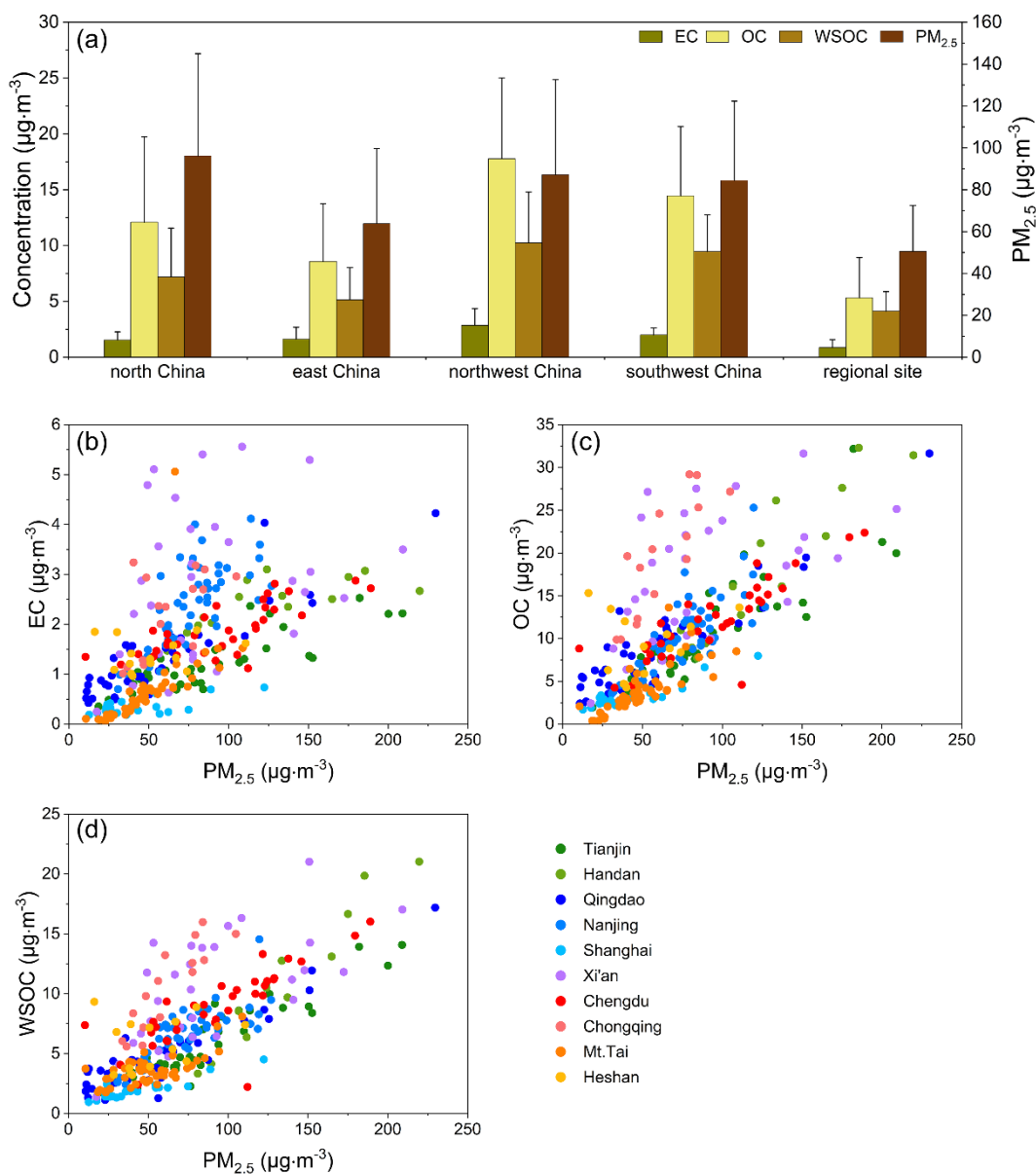
Figure S1. (a) Regional average carbonaceous component and PM$_{2.5}$ concentrations, and scatter plots of (b) EC, (c) OC and (d) WSOC with PM$_{2.5}$.
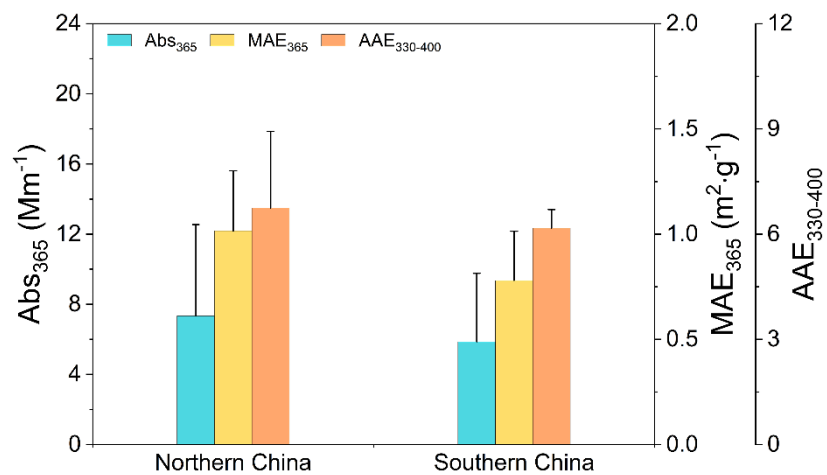
125   **Figure S2.** The average values of light absorption parameters (Abs_{365}, MAE_{365} and $AAE_{330-400}$) in Northern and Southern China.
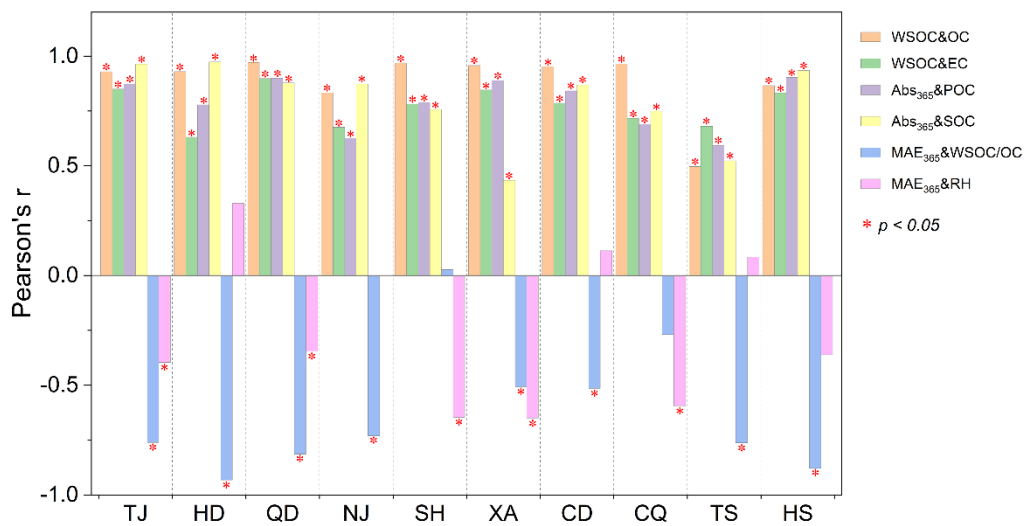
Figure S3. Pearson's correlation coefficients and significance levels (*p*, two-tailed) among different carbonaceous components, carbonaceous components and light-absorbing parameters, MAE$_{365}$ with RH at each site.
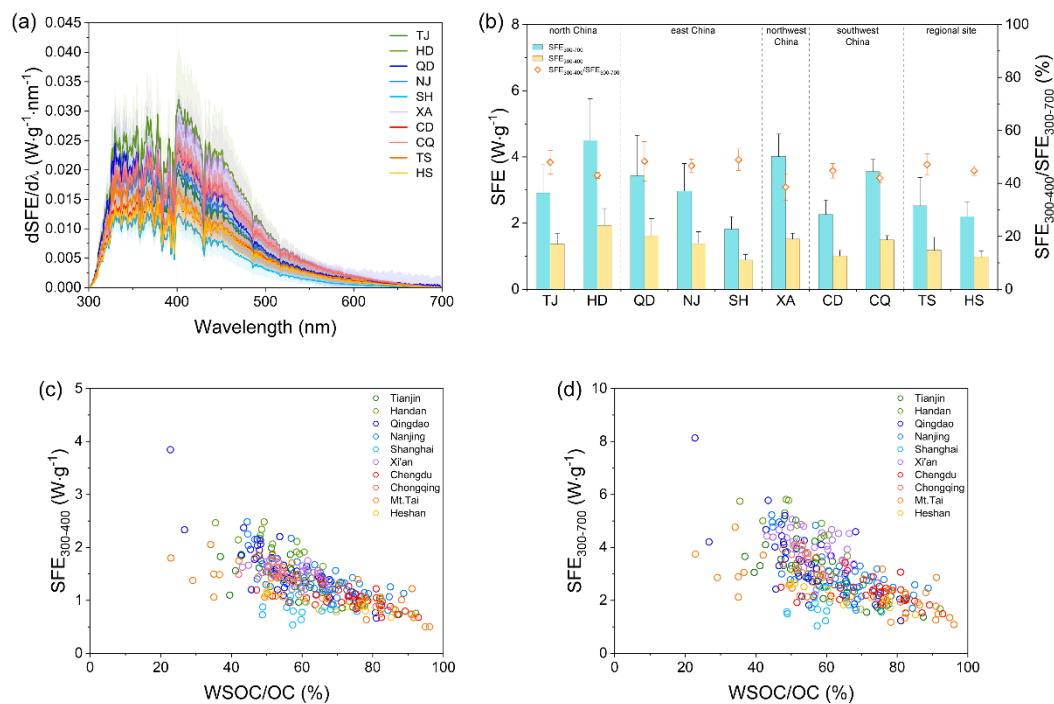
130   **Figure S4.** (a) SFE spectra of WSOC at different sites, (b) the integrated SFE values over the wavelength of 300-400 nm and 300-700 nm, (c) and (d) the scatter plots of the relationship between $SFE_{300-400}$ ($SFE_{300-700}$) and WSOC/OC.
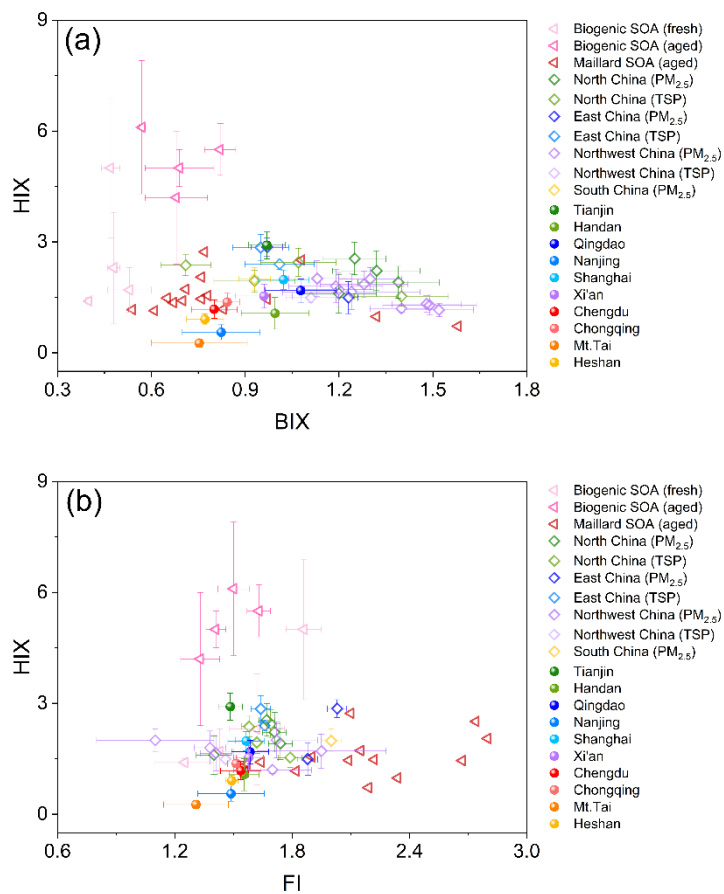
Figure S5. Scatter plots of HIX versus (a) BIX and (b) FI for WSOC measured in this study and reported in literatures (Deng et al., 2022; Li et al., 2023a; Wen et al., 2021; Zhan et al., 2022; Xie et al., 2020; Fan et al., 2023; Li et al., 2023b; Yu et al., 2023; Zhong et al., 2023; Qin et al., 2018; Zhang et al., 2021; Gao et al., 2021; Lee et al., 2013).
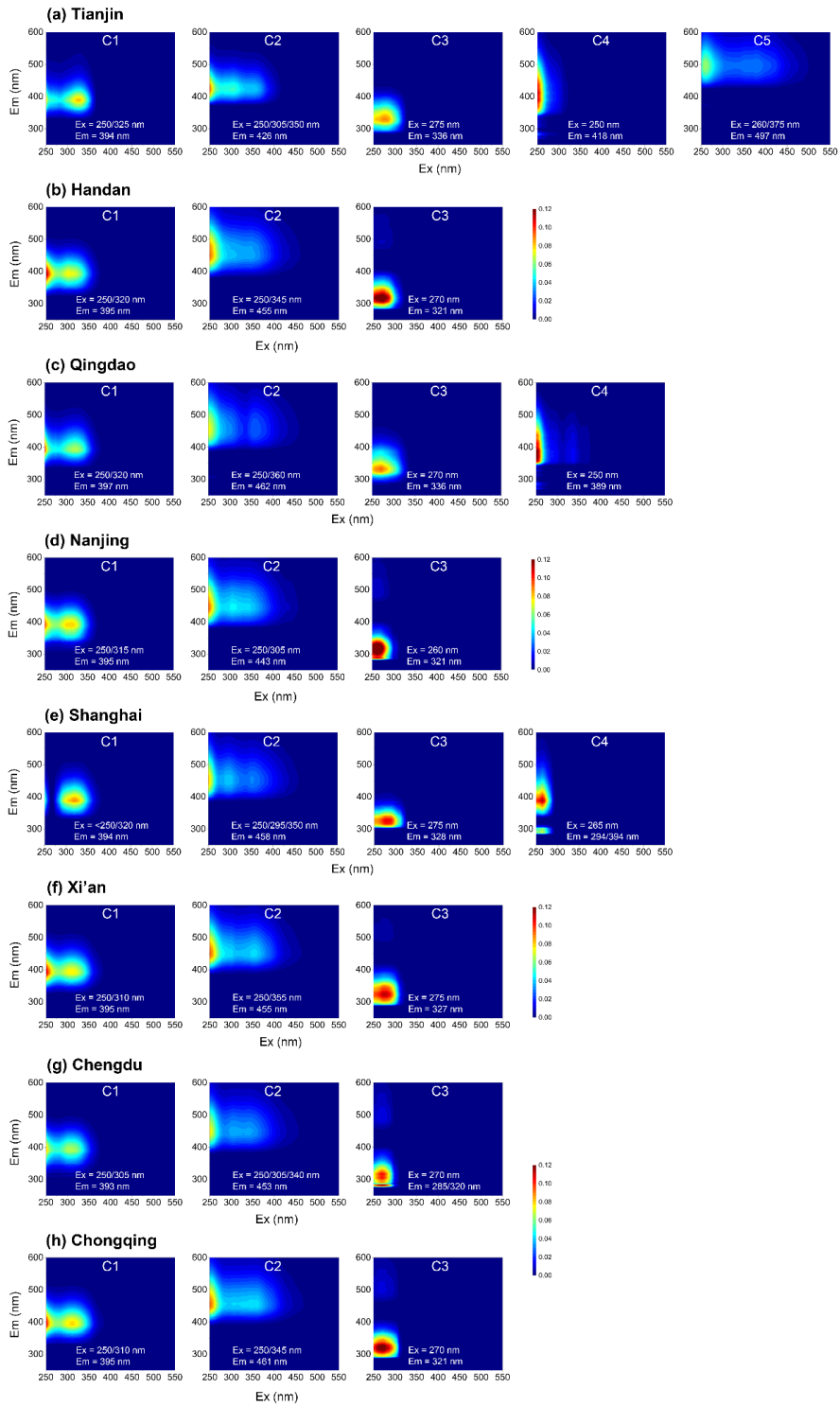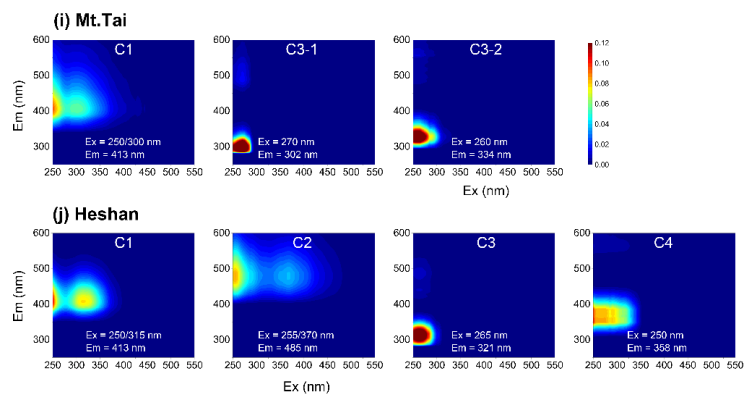
Figure S6. Fluorophores derived by PARAFAC in (a) Tianjin, (b) Handan, (c) Qingdao, (d) Nanjing, (e) Shanghai, (f) Xi'an, (g) Chengdu, (h) Chongqing, (i) Mt. Tai and (j) Heshan.
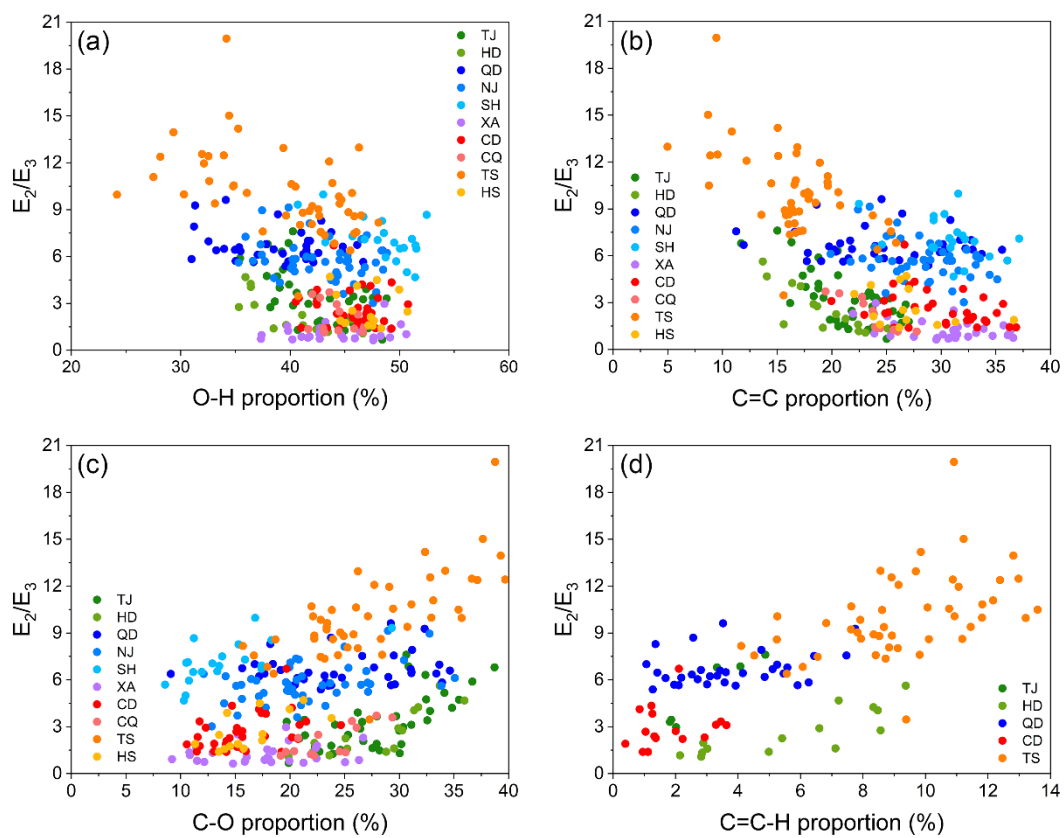
140

Figure S7. Scatter plots of the relative proportion of different functional groups (a) O-H, (b) C=C, (c) C-O and (d) C=C-H with E_2/E_3 value at each site.
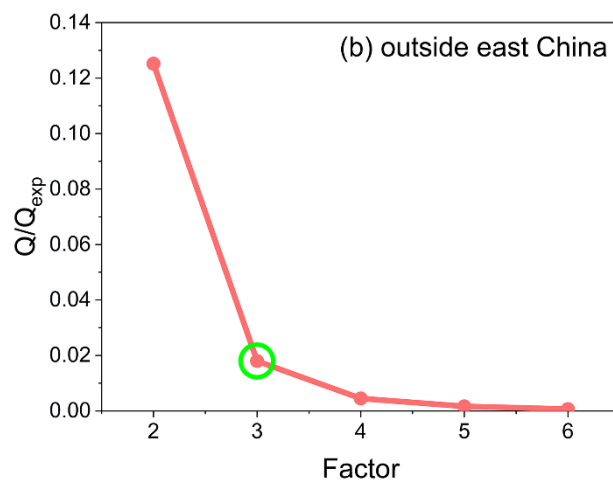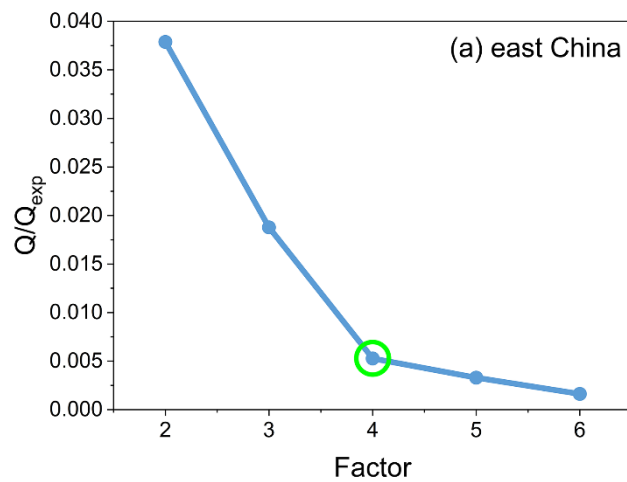
Figure S8. The $Q/Q_{expected}$ ratios of different factors in the PMF analysis for datasets collected in (a) east China and (b) outside east China.
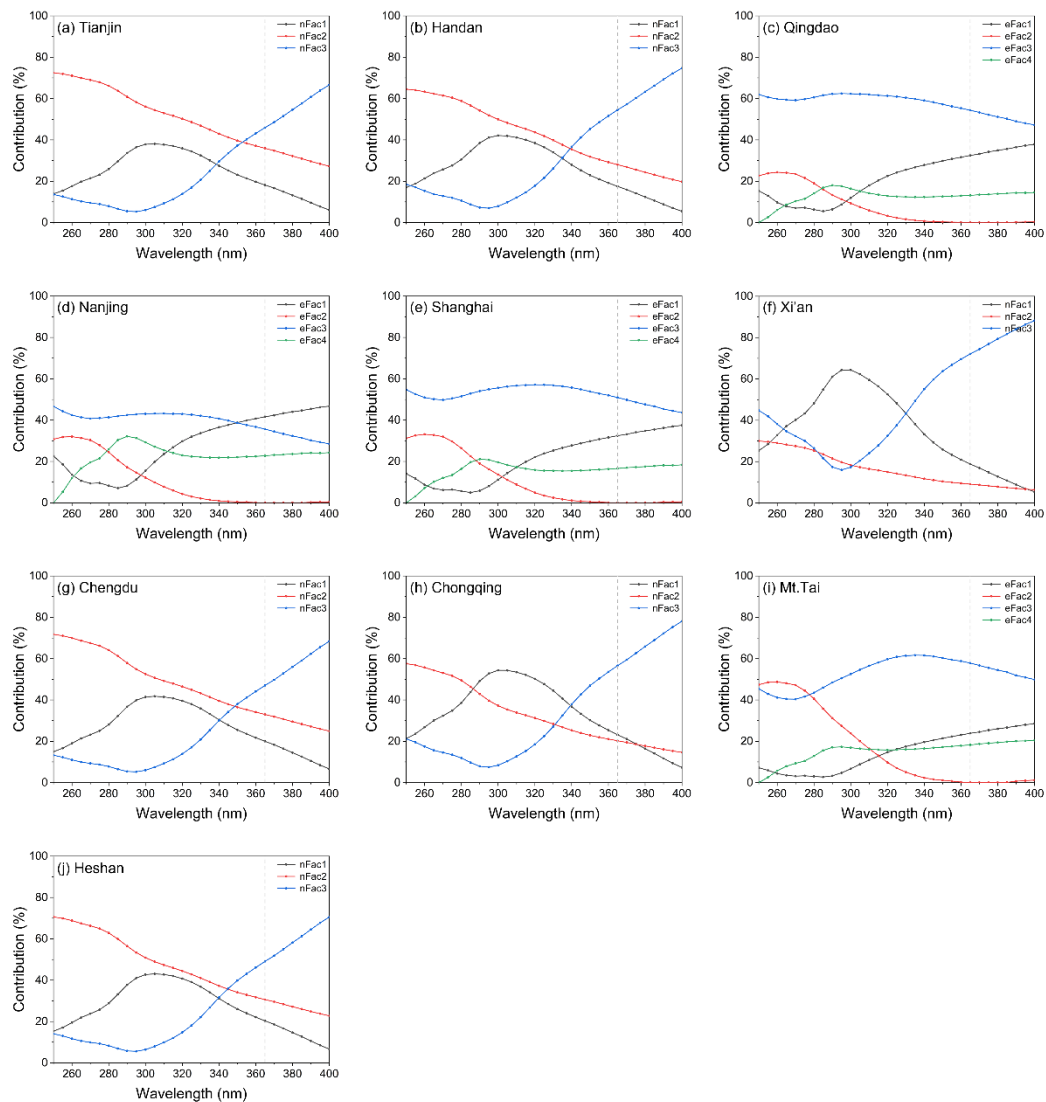
Figure S9. The proportion of different factors at different wavelengths for each site. Note: the dotted line represents the position of 365 nm.
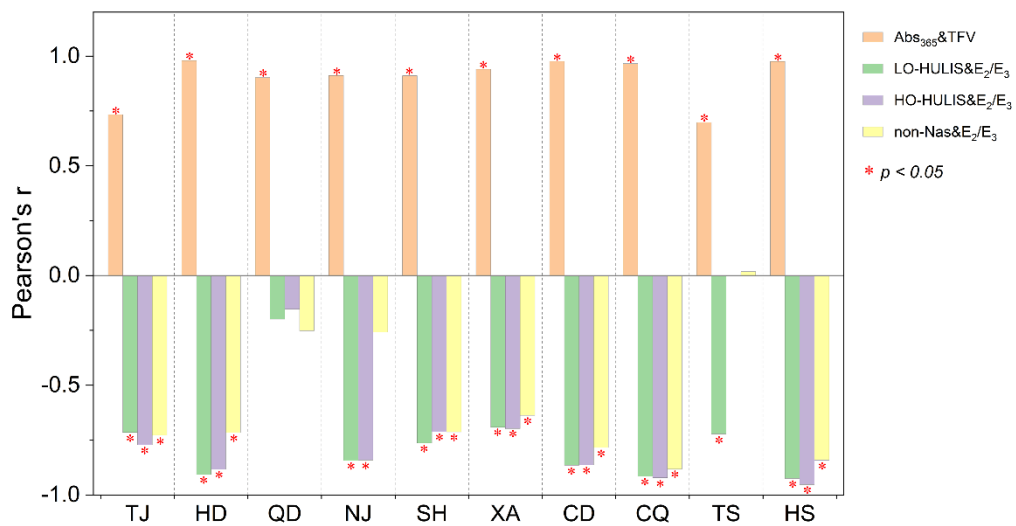
150 **Figure S10.** Pearson's correlation coefficients and significance levels (p, two-tailed) between Abs_{365} and TFV, E_2/E_3 and F_{max} of each fluorophore at each site.
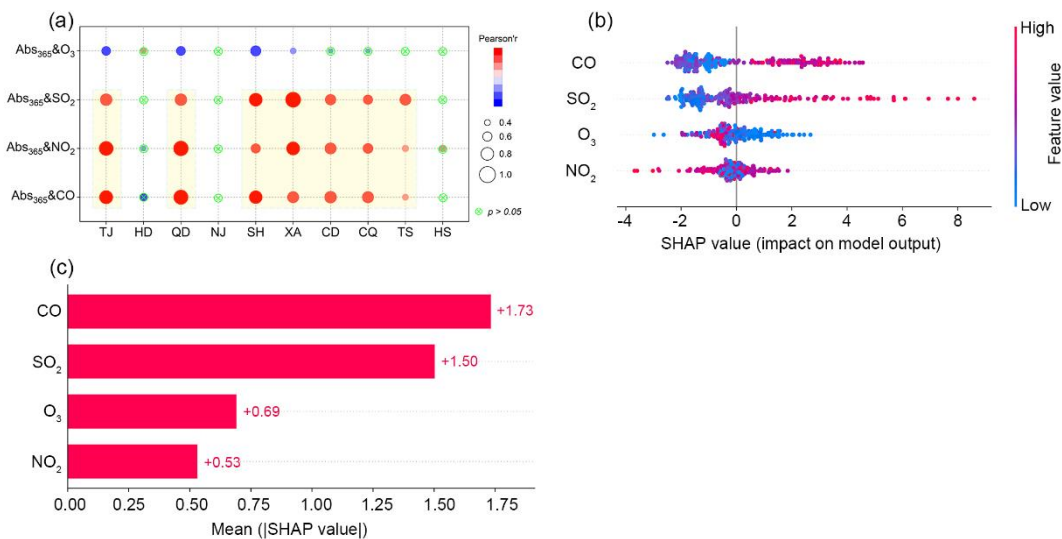
Figure S11. (a) Correlations between Abs_{365} and conventional air pollutants, and (b) SHAP summary plot (the color change of the scatter plot from blue to red indicates an increase in factor values), and (c) schematic of chemical component ordering, with SHAP values indicating the contribution of each factor to Abs_{365}.
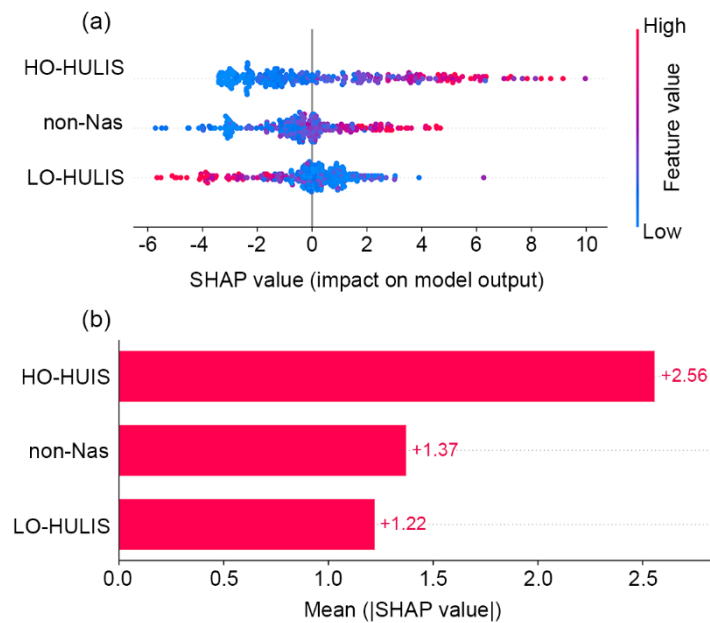
Figure S12. SHAP values calculated based on the XGBoost-SHAP model. (a) SHAP summary plot (the color change of the scatter plot from blue to red indicates an increase in factor values), (b) schematic of chemical component ordering with SHAP values indicating the contribution of each factor to Abs_{365}.

References

Deng, J., Ma, H., Wang, X., Zhong, S., Zhang, Z., Zhu, J., Fan, Y., Hu, W., Wu, L., Li, X., Ren, L., Pavuluri, C. M., Pan, X., Sun, Y., Wang, Z., Kawamura, K., and Fu, P.: Measurement report: Optical properties and sources of water-soluble brown carbon in Tianjin, North China-insights from organic molecular compositions, Atmospheric Chemistry and Physics, 22, 6449-6470, https://doi.org/10.5194/acp-22-6449-2022, 2022.

Fan, X., Cheng, A., Chen, D., Cao, T., Ji, W., Song, J., and Peng, P.: Investigating the molecular weight distribution of atmospheric water-soluble brown carbon using high-performance size exclusion chromatography coupled with diode array and fluorescence detectors, Chemosphere, 338, 139517, https://doi.org/10.1016/j.chemosphere.2023.139517, 2023.

Gao, Y., Wang, Z., Li, Y., Luo, H., and Zhou, Z.: Aqueous brown carbon formation by aldehyde compounds reaction with Glycine/Ammonium sulfate, Spectrochim Acta A Mol Biomol Spectrosc, 248, 119230, https://doi.org/10.1016/j.saa.2020.119230, 2021.

Lee, H. J., Laskin, A., Laskin, J., and Nizkorodov, S. A.: Excitation-emission spectra and fluorescence quantum yields for fresh and aged biogenic secondary organic aerosols, Environmental Science & Technology, 47, 5763-5770, https://doi.org/10.1021/es400644c, 2013.

Li, P., Yue, S., Yang, X., Liu, D., Zhang, Q., Hu, W., Hou, S., Zhao, W., Ren, H., Li, G., Gao, Y., Deng, J., Xie, Q., Sun, Y., Wang, Z., and Fu, P.: Fluorescence properties and chemical composition of fine particles in the background atmosphere of North China, Advances in Atmospheric Sciences, 40, 1159-1174, https://doi.org/10.1007/s00376-022-2208-x, 2023a.

Li, X., Yu, F., Song, Y., Zhang, C., Yan, F., Hu, Z., Lei, Y., Tripathee, L., Zhang, R., Guo, J., Wang, Y., Chen, Q., Liu, L., Cao, J., and Wang, Q.: Water-soluble brown carbon in PM2.5 at two typical sites in Guanzhong Basin: Optical properties, sources, and implications, Atmospheric Research, 281, 106499, https://doi.org/10.1016/j.atmosres.2022.106499, 2023b.

Qin, J. J., Zhang, L. M., Zhou, X. M., Duan, J. C., Mu, S. T., Xiao, K., Hu, J. N., and Tan, J. H.: Fluorescence fingerprinting properties for exploring water-soluble organic compounds in PM2.5 in an industrial city of northwest China, Atmospheric Environment, 184, 203-211, https://doi.org/10.1016/j.atmosenv.2018.04.049, 2018.

Wen, H., Zhou, Y., Xu, X., Wang, T., Chen, Q., Chen, Q., Li, W., Wang, Z., Huang, Z., Zhou, T., Shi, J., Bi, J., Ji, M., and Wang, X.: Water-soluble brown carbon in atmospheric aerosols along the transport pathway of Asian dust: Optical properties, chemical compositions, and potential sources, Science of the Total Environment, 789, 147971, https://doi.org/10.1016/j.scitotenv.2021.147971, 2021.

Xie, X., Chen, Y., Nie, D., Liu, Y., Liu, Y., Lei, R., Zhao, X., Li, H., and Ge, X.: Light-absorbing and fluorescent properties of atmospheric brown carbon: A case study in Nanjing, China, Chemosphere, 251, 126350, https://doi.org/10.1016/j.chemosphere.2020.126350, 2020.

Yu, F., Li, X., Zhang, R., Guo, J., Yang, W., Tripathee, L., Liu, L., Wang, Y., Kang, S., and Cao, J.: Insights into dissolved organics in non-urban areas - Optical properties and sources, Environ Pollut, 329, 121641, https://doi.org/10.1016/j.envpol.2023.121641, 2023.

Zhan, Y., Tsona, N. T., Li, J., Chen, Q., and Du, L.: Water-soluble matter in PM2.5 in a coastal city over China: Chemical

components, optical properties, and source analysis, journal of Environmental Sciences, 114, 21-36, https://doi.org/10.1016/j.jes.2021.07.011, 2022.

Zhang, C., Chen, M., Kang, S., Yan, F., Han, X., Gautam, S., Hu, Z., Zheng, H., Chen, P., Gao, S., Wang, P., and Li, C.: Light absorption and fluorescence characteristics of water-soluble organic compounds in carbonaceous particles at a typical remote site in the southeastern Himalayas and Tibetan Plateau, Environmental Pollution, 272, 116000, https://doi.org/10.1016/j.envpol.2020.116000, 2021.

Zhong, M., Xu, J., Wang, H., Gao, L., Zhu, H., Zhai, L., Zhang, X., and Zhao, W.: Characterizing water-soluble brown carbon in fine particles in four typical cities in northwestern China during wintertime: integrating optical properties with chemical processes, Atmospheric Chemistry and Physics, 23, 12609-12630, https://doi.org/10.5194/egusphere-2023-752, 2023.